Use of infrared microspectroscopy to elucidate a specific chemical signature associated with hypoxia levels found in glioblastoma†

Christophe Sandt,*[a] Céline Nadaradjane,[a,b] Rosalie Richards,[b] Paul Dumas[a] and Violaine Sée[b]

Hypoxia is a common feature of solid tumours and is associated with poor prognosis, resistance to radio- and chemotherapy, and tumour aggressiveness. For predictive purposes as well as for improved therapeutic intervention, it is increasingly needed to have direct and specific diagnostic tools in order to measure the extent of, and changes in, tumour hypoxia. In this article, we have investigated the potential of Fourier Transform Infrared (FTIR) microspectroscopy, at cellular and subcellular resolution, for detecting hypoxia-induced metabolic changes in brain tumour (glioblastoma) cell lines and in short term primary cultures derived from patient samples. The most prominent and common changes observed were the increase in glycogen (specifically in the U87MG cell line) and lipids (all cell lines studied). Additionally, each cell line presented specific individual metabolic fingerprints. The metabolic changes did not evolve markedly with time (from 1 to 5 days hypoxic incubation), and yet were harder to detect under chronic hypoxic conditions, which is consistent with cellular adaptation occurring upon long term changes in the microenvironment. The metabolic signature was similar regardless of the severity of the hypoxic insult and was replicated by the hypoxia mimetic drug dimethyloxalylglycine (DMOG). To investigate any specific changes at subcellular levels and to improve the sensitivity of the detection method, spectra were recorded separately in the cytoplasm and in the nucleus of D566 glioblastoma cells, thanks to the use of a synchrotron source. We show that this method provides improved detection in both cell compartments. Whilst there was a high spectral variability between cell lines, we show that FTIR microspectroscopy allowed the detection of the common metabolic changes triggered by hypoxia regardless of cell type, providing a potential new approach for the detection of hypoxic tumours.

[a]Synchrotron SOLEIL, L'Orme des Merisiers, 91192 Gif sur Yvette, France. E-mail: sandt@synchrotron-soleil.fr
[b]Department of Biochemistry, Institute of Integrative Biology, University of Liverpool, Liverpool, UK
†Electronic supplementary information (ESI) available. See DOI: 10.1039/c5an02112j

Introduction

The tumour microenvironment, and in particular the low oxygen levels found in solid tumours, plays a critical role in their development and aggressiveness.[1] Indeed, tumour hypoxia has been extensively described as associated with radio- and chemotherapy resistance as well as with increased metastatic properties.[2–4] Such acquired phenotypes are essentially triggered by the transcription of a number of genes orchestrated by the transcription factor Hypoxia Inducible Factor (HIF). As a matter of fact, high HIF levels have been associated with bad prognosis for many solid tumours.[5–11] However, HIF is not an ideal marker of tumour hypoxia, for both technical and biological reasons.[4,12] Antibody-based detection poses the problem of sensitivity and specificity of the antibody and immuno-labelling, and relies heavily on antibody quality. Moreover, HIF levels are dynamically regulated due to the presence of negative feedback loops in the signalling module[13] and their transiency means that HIF levels may not be directly correlated with cellular hypoxia.[12] Moreover, HIF levels can be increased by factors other than hypoxia,[14–16] again pointing to a potential lack of correlation between HIF and the extent of hypoxia. None of the other putative molecular markers of hypoxia (*e.g.* HIF2, VEGF, EF5, GLUT1, CA9) is exclusively hypoxia-specific.[17–19] Nitroimidazole compounds such as pimonidazole have previously been used to monitor tissue hypoxia, yet have major drawbacks such as the requirement of their administration to the patient prior to detection, and low correlation with other hypoxia markers.[20] As such, there is a crucial need for being able to directly and non-invasively detect the extent of tumour hypoxia in order to improve patient outcome prediction and therapeutic strategies.

The hypoxic state is not only characterized by the expression of transcription factors, but also by metabolic changes such as a shift from high-energy to low-energy phosphate ratio, up regulation of glycolysis,[21,22] increased glucose uptake, changes in triglyceride and steroid levels, and accumulation of lipid micro-droplets.[23] Many of these changes can be detected by infrared spectroscopy, a method that probes the specific infrared absorptions by molecular bond motions. We hypothesized that infrared spectroscopy may be able to detect hypoxia specific metabolic changes in tumours and be used as a tool to measure hypoxia in tumour samples. Tumours are highly heterogeneous, with hypoxic, normoxic and necrotic regions,[8,19,24] and the use of an infrared microscope would allow the collection of spatially resolved information in tumour biopsies, thereby avoiding misleading global measurements.

The infrared spectrum of a molecule is a fingerprint of the nature, composition, and conformation of a given molecule. It is a particularly sensitive method for detecting lipids, proteins and carbohydrates in tissues.[25–27] The infrared spectrum of a cell or tissue is not only a fingerprint of its chemical composition, but also of its nature,[28–30] physiological status,[31,32] and position in the cell cycle,[33] and can therefore be used to monitor physiological or pathological changes.[34–36] Cells are composed of around 70% proteins (dry w/w), while metabolites only represent 3% of a cell mass. Therefore, infrared spectroscopy will preferentially probe concentrations of the main macromolecules whilst low levels of metabolites such as lactate or pyruvate are less likely to be detected in an intact cell. Since most cells or tissues do not undergo major metabolic changes, sophisticated pattern recognition techniques are used to detect and monitor the subtle changes in cell spectral signatures and classify the spectra objectively. In hypoxia, where a strong metabolic reprogramming occurs, with changes in cell lipid and carbohydrate quantity and composition, the sensitivity of infrared detection seems particularly suitable. Coupling the infrared microscope to a synchrotron source can provide subcellular resolution and the ability to study the chemical changes of specific cell compartments, which may be important when organelle specific events are expected (e.g. during cellular respiration).

In this study we have used synchrotron radiation infrared microspectroscopy to study the chemical composition of cells cultured at several oxygen tensions and culture durations, on whole individual cells, and at subcellular resolution in the cytoplasm and nucleus. We have shown that metabolic changes triggered by hypoxia can be detected irrespective of the severity and duration of hypoxia, yet some of the changes are subtle and/or cell line specific.

Experimental

Cell culture and hypoxic incubation

Cell lines. HeLa cells, U87MG and D566 human cell lines were used in this study. HeLa cells are epithelial cells derived from the cervical adenocarcinoma of a human female. U87MG are astrocytoma cells derived from a grade IV glioblastoma from human brain and adopt an epithelial morphology. D566 cells were derived from a glioblastoma from the brain of a human patient and also adopt an epithelial morphology. U87MG were obtained from ATCC (Teddington, UK), HeLa cells from ECACC (Salisbury, UK) and the D566 cells were a kind gift from Professor D. D. Bigner (Duke University Medical Centre, USA). U87MG and D566 cells were maintained in MEM supplemented with 1% sodium pyruvate (Life Technologies) and 10% FCS (PAA). D566 cells were also supplemented with 1% non-essential amino acids (NEAA, Life Technologies). HeLa cells were maintained in MEM plus 10% FCS and 1% NEAA. All cells were maintained at 37 °C, under 5% CO_2.

Short term primary cell culture. Samples of primary glioblastoma (GBM) tumours were received from patients undergoing craniotomy and resection, who had given informed written consent to donate their tissue to the Walton Research Tissue Bank, Walton Centre NHS Foundation Trust. Samples were mechanically dissociated in MEM plus 1% penicillin–streptomycin on a Petri dish before being transferred into dissociation medium (10% trypsin 10X and 1% DNAse in MEM plus 1% penicillin–streptomycin). The sample was incubated for 15–30 min at 37 °C and triturated every 5 min. When a homogeneous suspension was achieved the trypsin reaction was stopped by adding 10 mL of growth medium. Cells were centrifuged for 5 min at 3000 rpm to remove red blood cells and debris. The pellet was re-suspended in growth medium and seeded into a 75 cm^2 tissue culture flask. Cells were used for experiments between passages 2 and 5.

Hypoxic incubation and DMOG treatment. Prior to plating on CaF_2 coverslips, cells were counted using a Bio-Rad TC20 automated cell counter and seeded at a density of 5×10^5 cells per mL. Cells exposed to 1% O_2 were cultured in a Don Whitley H35 Hypoxystation, and cells exposed to 0.1% O_2 were incubated in a New Brunswick Galaxy 48R hypoxic incubator. When indicated, normoxic cells where treated with 0.5 mM dimethyloxalylglycine (DMOG) for 24 h to mimic hypoxia.

Cell preparation for FTIR microspectroscopy. Cells were measured directly on the CaF_2 coverslips. After incubation, cells were fixed in 4% formalin for 10 minutes, then rinsed with distilled water and dehydrated at room temperature under a laminar flow hood.

FTIR microspectroscopy

Spectra were recorded at the SOLEIL synchrotron facility on the SMIS beamline, using the edge and constant field radiation of a bending magnet.[37] The synchrotron delivers 430 mA current in the 4/4 filling and 3/4 hybrid modes and runs in the top-up mode for injection (delivering near constant intensity).

Spectra were recorded in a transmission mode on a Nicolet Continuum XL microscope (Thermo Fischer, Courtaboeuf, France) equipped with a 50×50 μm^2 liquid-nitrogen cooled MCT/A detector, a 32×/NA 0.65 Schwarzschild objective and a matching 32× condenser, and a Prior Proscan XYZ motorised stage. The microscope was coupled to a Nicolet 5700 spectrometer (Thermo Fischer, Courtaboeuf, France) equipped with a Michelson interferometer and a KBr beamsplitter. The spectro-

meter and the microscope were continually purged with dry air from a Parker-Balston FT-IR purge gas generator for atmospheric control. The microscope was operated in a single aperture mode and the knife-edge aperture was set at 20×20 μm^2, for recording the spectra of whole cells, and at 10×10 μm^2 for recording the spectra of nuclei and cytoplasms. Spectra were recorded with 128 scans at 4 cm^{-1} resolution. Spectral maps were recorded by raster scanning the cells with steps of 3 μm in both directions with a projected aperture size of 6×6 μm^2. The background spectrum was recorded from a clean spot on the CaF$_2$ coverslip close to the measured cells. A new background was collected after one hour.

Sampling

At least 50 cells per sample were deemed necessary for statistical significance, so we collected between 60 and 100 spectra per sample to ensure that an adequate number of spectra were of satisfactory quality for statistical treatment. Cells with obvious Mie scattering causing features (single isolated round cells, spherical cells protruding from a flat smear, or cells with pyknotic nuclei) were not measured. These cells are generally apoptotic and their spectral signatures are not representative of the population. Under all conditions tested, apoptosis remained below 10%.

Spectra were sorted by visual examination and by multivariate statistical analysis to eliminate those that displayed anomalies in their overall shape (Mie scattering, misalignment, etc.).

Replicate cell cultures were measured for each condition, with the exception of primary cell cultures.

For subcellular resolution measurements, spectra were recorded from at least 50 nuclei and 50 cytoplasms for each sample, and analysed by Principal Component Analysis (PCA) and difference spectroscopy.

Spectrum sorting

As stated above, spectra were sorted by visual inspection, prior to further selection by a multivariate approach based on PCA. Spectra with artefacts that could not be corrected by the available algorithms were eliminated prior to pretreatment and statistical analysis. For eliminating Mie scattered spectra, the following rejection criteria were used: splitting of the 1740 cm^{-1} C=O band from amide I, position of the amide I band below 1650 cm^{-1}, baseline offset, sine baseline shape, intensity of shoulder at 1640 cm^{-1} in amide I above half height, intensity of the shoulder at 1515 cm^{-1} in amide II, width of the amide II, splitting between the amide II band and the CH bending modes. Remaining outlier spectra were identified using multivariate statistical tools in The Unscrambler X 10.3 (Camo Inc., Norway). The Hotelling T2 ellipse and the influence plot were used to remove the remaining outliers after a first PCA round; spectra with high residuals and high weight for the principal components collating up to 90% of the variance were removed, as were spectra out of the 95% Hotelling T2 ellipse and not connected to spectra within the ellipse.

Chemical maps

Chemical maps were generated with Omnic software (Thermo-Fischer, Courtaboeuf, France) by plotting the integrated inten-

sity of the specific band area. A linear baseline correction within the wavenumber range of the band was included in the integration procedure. The limits for integration are given in Table 1 together with main band assignments observed between 950 and 4000 cm^{-1}. The infrared spectrum is separated into two regions: the CH range on one hand (2800–3030 cm^{-1}), which contains mainly absorptions from C–H stretching vibrations of lipids, and proteins, and the fingerprint range on the other hand (950–1800 cm^{-1}), which contains absorptions of stretching and deformation vibrations from C=O, C–O, N–H, C–H, C–N, C–C, P=O bonds.

Pretreatments prior to multivariate analysis

Spectra were treated prior to analysis to eliminate sources of variation, such as differences in cell thickness and light scattering properties. All pretreatments were carried out in The Unscrambler X 10.3.

Spectra were corrected by Extended Multiplicative Scattering Correction (EMSC) in the fingerprint region or in the CH region. First or second derivative spectra were systematically computed for correcting baseline distortions, to improve the resolving power and to check consistency with EMSC treated data. Derivatives are presented whenever EMSC failed to give the tightest clustering. First, a Savitzky–Golay smoothing was performed (polynomial order 3, 9 or 21 points), and then a Savitzky–Golay derivative filter was applied (polynomial order 3, 13 or 15 points). Unit Vector Normalisation (UVN) was carried out to normalize the spectra. Since derivative spectra become difficult to interpret (especially when analysing with PCA), difference spectra were calculated for interpreting chemical changes between samples, provided that the spectra had a unimodal distribution which was generally the case.

Principal component analysis

Because the differences between hypoxic and normoxic cell spectra were expected to be subtle and hundreds of spectra were needed for comparison and objective classification, computerised pattern recognition methods were used. Spectra were analysed by PCA, a multivariate statistical analysis that seeks to express a large number of correlated variables as a smaller number of orthogonal (independent) components. PCA allows an easier overview of the data structure (evidencing whether groups exist), explains relationships between variables (redundancies, correlations and anti-correlations), and unravels subtle changes that are hidden by the most evident variations. The results of PCA can be given as a graphical output with two types of plots. Score plots, where each spectrum is represented by a point and similar spectra are clustered together, are used to detect the presence of groups (data structure). Loadings plots show the 'principal components', linear combinations of the original spectral variables that explain the chemical information behind the data structure. As principal components are independent, they can reveal uncorrelated sources of variation.

PCA was performed in The Unscrambler X 10.3 on mean centered data. Pretreated spectra were analysed independently

Table 1 Putative assignment of the bands found in the infrared spectra of glioblastoma cells

Band assignment between 950 and 4000 cm^{-1}

Position (cm^{-1})	Vibration	Integration limits	Chemical moieties	
Proteins				
3300	ν NH		Amide A	
3070			Amide B	
2960	ν C–H	3000–2950	CH$_3$ from amino acids	
1654	ν C=O, C–N, N–H	1720–1590 cm^{-1}	Amide I	Combination bands from the protein backbone
1540	δ N–H, C–N, C–C, C–O		Amide II	
1200–1380	δ N–H bend, ν C–N		Amide III	
Lipids				
3010	ν C=C–H		Unsaturated fatty acids	
2954	ν_{as} C–H	3000–2950	CH$_3$ from fatty acids	
2922	ν_{as} C–H	2905–2945	CH$_2$ from fatty acids	
2875	ν_{sym} C–H		CH$_3$ from fatty acids and proteins	
2850	ν_{sym} C–H		CH$_2$ from fatty acids	
1740	ν C=O	1720–1780	C=O from lipid esters and phospholipids	
1465	δ C–H		CH$_2$ from fatty acids	
1452	δ C–H		CH$_2$ from fatty acids	
1440	δ C–H		CH$_2$ cyclic	
1380	δ C–H		CH$_3$ from fatty acids	
1365	δ C–H		CH$_2$ from fatty acids	
1220–1230	ν_{as} P=O		Phospholipids	
1170–1180	ν_{as} C–O		Phospholipids	
1080–1090	ν_{sym} P=O		Phospholipids	
Polysaccharides				
3420	ν O–H		C–OH	
1400	COO$^-$		Carboxylic acids	
1150	ν_{as} C–O, ν_{as} C–C	1000–1180	C–OH, C–OC, C–C	Glycogen, glucose, ribose, carbohydrates, protein glycosylation
1120–1130	ν_{as} C–O, ν_{as} C–C		C–O, C–C	
1075–1085	ν_{sym} C–O, ν_{sym} C–C		C–OH, C–OC, C–C	
1045–1060	ν_{sym} C–O		C–OH	
1040	ν C–O of C–OH		Ribose	
1025	δ C–O, ν C–O of CH$_2$OH		Glycogen	
Nucleic acids				
1420	δ C–H		Deoxyribose	
1370	C–N		Deoxythymidine	
1240	ν_{as} P=O PO$_2$	1195–1275	A form DNA backbone	
1215	C–C–O–C		Ribose	
1105	ν C–O		Ribose	
1085	ν_{sym} P=O PO$_2$		DNA backbone	
960–970	ν C–O, C–C		DNA backbone, deoxyribose	

ν: stretching vibration, δ: bending vibration, as: asymmetric vibration, sym: symmetric vibration.

in the two frequency domains. Six principal components were computed by the NIPALS algorithm with leverage correction. Two rounds of PCA were systematically performed; the first round was used to detect and eliminate remaining outliers, the second round was used to analyse the data structure. When relevant, the Varimax rotation was applied to collate the most significant principal components (PC) in a single PC.

Calculation of spectral differences

The most typical spectra for each group (those located in the centre of the PCA cloud) were extracted and used to calculate an average spectrum representative of that group. Typically 35 to 50 spectra were used for each group. Difference spectra were computed by subtracting the mean normoxic spectrum from the mean hypoxic spectrum and multiplying by ten.

Results

Hypoxic cells can be differentiated from normoxic cells by their infrared spectra

We first aimed at investigating if the infrared spectra of cells cultured in atmospheric O$_2$ levels (21% O$_2$, here called normoxia) could be altered by culturing the same cells at 1% O$_2$, a typical O$_2$ level found within the tumour mass.[38,39] We used 2 glioblastoma cell lines (U87MG and D566) since glioblastoma are well described as hypoxic tumours and we compared

them to the widely used HeLa cells. Primary cells cultured from glioblastoma tissue acquired at resection were also analysed. Fig. 1 shows the result of PCA carried out on U87MG cell spectra. In the score plot (Fig. 1A), hypoxic cell spectra can be separated from normoxic cell spectra along the principal component 1 (PC1) axis. Approximately 87% of normoxic and 92% of hypoxic cell spectra are correctly separated. The structure of the data shows continuity between the hypoxic and normoxic cell spectra with an overlapping of the 2 groups, meaning that some of the hypoxic cells have phenotypic features of normoxic cells. The loadings plot in Fig. 1A shows negative peaks at 1740, 1465, 1455, and 1380 cm^{-1}, which is interpreted as an increase in the lipid signal in the hypoxic cells, and negative peaks at 1155, 1080 and 1025 cm^{-1}, which are due to an increase in the carbohydrate signal in the hypoxic cells. The profile of the carbohydrate signal is similar to that of glycogen suggesting an increase in glycogen storage in hypoxic U87MG cells. Varimax rotation was used to collate all the spectral variance between normoxic and hypoxic cell spectra into one principal component that accounted for 30% of the spectral variance. The remaining 70% variance was not relevant for separating between the 2 groups. The two groups appear relatively homogeneous; 4 spectra from the hypoxic groups (indicated by arrows in Fig. 1A) are clustered apart from the rest of the hypoxic cells along the PC1 axis. Upon inspection these spectra present high levels of glycogen and lipids. Similar levels of glycogen were previously found in hepatocytes[40] and in stem cells.[28,41] Since the data structure appears unimodal for each group, average spectra can be used to represent the mean of each of the 2 cell populations (Fig. 1B). The difference spectrum shows positive peaks at 1735, 1465, 1455, 1155, 1080, and 1025 cm^{-1}, evidencing an increase in lipid and glycogen signals in hypoxic cells at 24 h.

The same analysis was carried out for HeLa, D566 and primary GBM cells. The PCA score plots and loadings plots are shown in ESI Fig. S1† and the results are recapitulated by the difference spectra in Fig. 1C–E. For each of these cell types, hypoxic and normoxic cell spectra can be separated in PCA. Different spectral ranges and data preprocessing were used for obtaining the best separation depending on the variations in the original data. The spectral differences in the fingerprint region (Fig. 1B–E) show that the spectral signature of the hypoxic cells is different in each cell line compared to its normoxic counterpart. Only U87MG cells presented an obvious increase in the glycogen signal (Fig. 1B), suggesting an imbalance between the increased glucose uptake and glucose usage, which results in glycogen storage. Changes in the carbohydrate region (950–1180 cm^{-1}) in HeLa, D566 and primary GBM cells were more subtle, potentially due to a tighter balance between glucose uptake and glycolysis in these cells (Fig. 1C–E). All hypoxic cells presented an increase in the lipid signal that could be detected by an increase of the C=O peak at 1740 cm^{-1}, and C–H peak at 1465 cm^{-1}, in U87MG, HeLa and primary GBM cells (Fig. 1B, D and E), and at 1170 cm^{-1} in primary GBM cells only (peak hidden by the C–O from carbohydrates in other cell lines). Moreover, there is an increase of

the C–H signal at 2920 and 2850 cm^{-1} in U87MG (data not shown), D566 (Fig. S1A†) and HeLa (Fig. S1B†) cells. Small changes in the profile of the protein bands were also detected in all cell lines but no common feature could be observed for the protein signal. The increase in lipid and carbohydrate signals observed in most cells is commensurate with known modifications of hypoxic cell metabolism such as lipid droplet accumulation[23] and increased expression of the GLUT1/3 glucose transporters.[6,42,43] In summary, each cell line seemed to have a slightly different hypoxic signature, yet the increase in the lipid signal was clearly a common feature for all cell lines.

Severe hypoxia induces the same metabolic changes as mild hypoxia

To assess if the spectral changes induced by hypoxia could be dependent on the severity of the hypoxic switch, glioblastoma cells were grown for 24 h in 0.1% O_2, a level of O_2 which has been reported in certain regions of solid tumours.[44] Although this level of hypoxia is severe, short term exposure (<48 h) does not compromise cell survival (Richards *et al.*, submitted). The FTIR spectra were then compared with cells grown for 24 h at 21% O_2. It was possible to separate normoxic from hypoxic cells by PCA as shown in Fig. 2 (D566 cells) and ESI Fig. S2† (U87MG and primary GBM). Fig. 2A shows the score plot of the PCA carried out in the fingerprint region on second derivative spectra. Hypoxic and normoxic cell spectra can be almost perfectly separated by PC3 carrying 12% of the spectral variance. Since loadings are difficult to interpret when using the second derivative spectra, the difference spectrum was calculated (Fig. 2B) and the difference spectra of mild hypoxia and severe hypoxia are compared in Fig. 2C. The overall shape of the 2 difference spectra was the same, with the main variation coming from baseline drift. Peaks at 1720, 1620–1630, 1400, 1370, and 1225 cm^{-1} could be observed in both difference spectra. Subtle differences in the carbohydrate regions are seen at 1145, 1100, and 1045 cm^{-1} related to the C–O stretching vibrations and were difficult to interpret, but could result from small differences in the glucose/glycogen balance and in the expression level of various glycoproteins.

The signatures of primary GBM cells and U87MG cells incubated in severe hypoxia closely resemble those of their mild hypoxia counterparts, with strong C=O, C–H and C–OH signals in the primary GBM difference spectrum (Fig. 2D and S2B†). There is also a clear glycogen signature in the U87MG difference spectrum (Fig. 2E and S2B†). Surprisingly, severe hypoxia did not seem to induce a change in the data structure such as a total separation between the hypoxic and normoxic cell spectra clusters in PCA (Fig. 2A, S2A and S2B†). We observed an overlap between the hypoxic and normoxic clusters, and few cells were not separated as with mild hypoxia. This suggests that severe hypoxia does not cause stronger metabolic changes that can be detected by infrared spectroscopy.
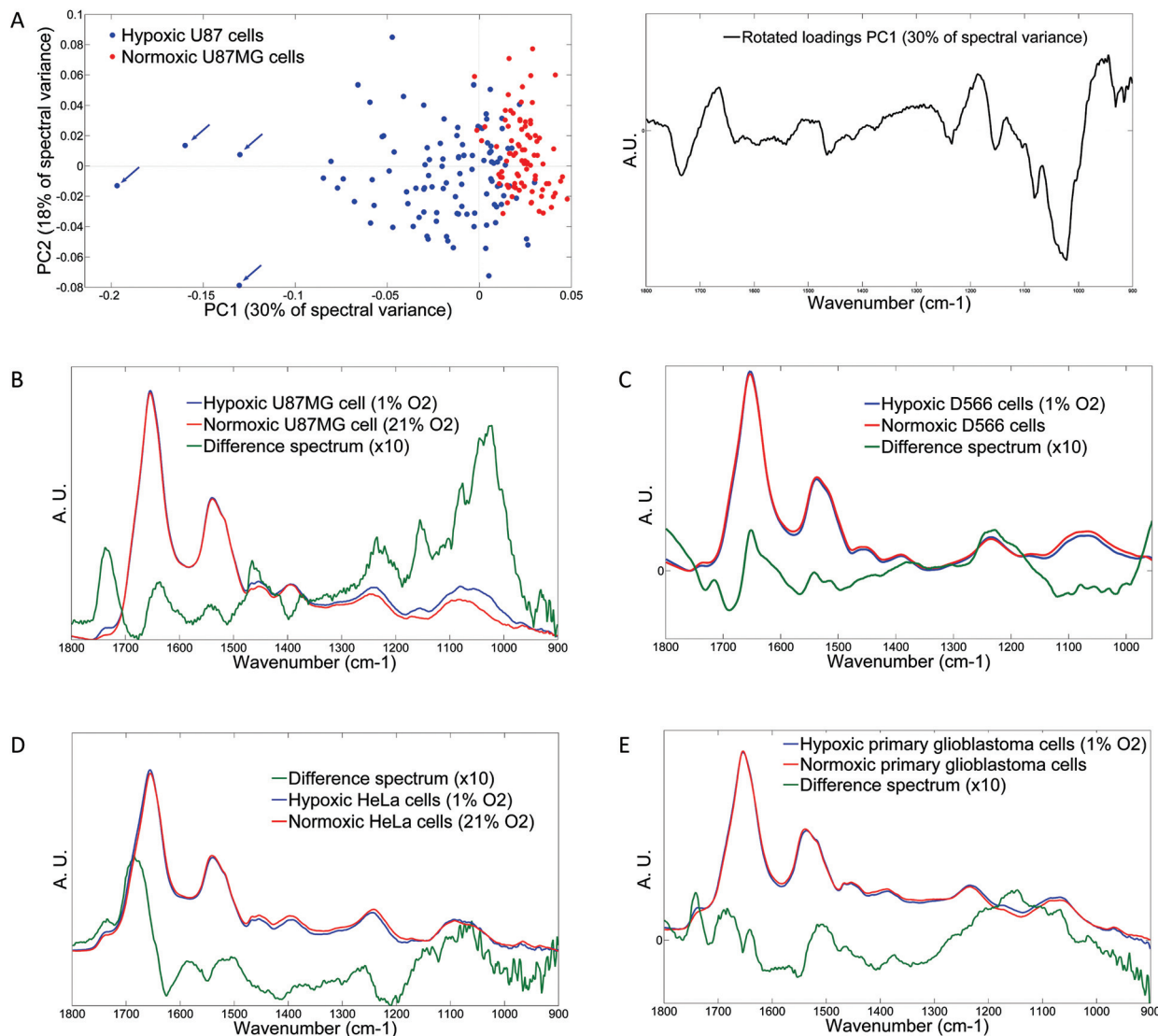
Fig. 1   Cells grown under hypoxic conditions (1% O_2) can be differentiated from normoxic cells (21% O_2) by their infrared spectra at single cell resolution. (A) Analysis of U87MG cell spectra by Principal Component Analysis (PCA) in the fingerprint (900−1800 cm^{-1}) region. Left: score plot, right: loadings plot. U87MG glioblastoma cells were grown for 24 h in normoxia (21% O_2) or hypoxia (1% O_2). The hypoxic (red) and normoxic (blue) cell spectra can be separated along the PC1 axis. The arrows mark 4 cell spectra with extremely high levels of lipids and glycogen. (B) Average spectra of U87MG cells after 24 h at 21% (red) and 1% (blue) O_2. The spectral difference (green) shows signals from glycogen (1150, 1080 and 1025 cm^{-1}) and weaker contribution from lipids (1740, 1460, and 1370 cm^{-1}) and phosphates (1240 cm^{-1}). (C) Average spectra of D566 glioblastoma cells after 24 h at 21% (red) and 1% (blue) O_2. The spectral difference (green) shows changes in the lipids, protein amide I and II, phosphate, and carbohydrate regions. (D) Average spectra of HeLa cells after 24 h at 21% (red) and 1% (blue) O_2. Spectral differences (green) arise mainly in the C═O at 1740 cm^{-1}, protein amide I and amide II bands and in the large CO band between 1180 and 900 cm^{-1}, suggesting changes in the glycoproteins. (E) Average spectra of primary GBM cells after 24 h at 21% (red) and 1% (blue) O_2. The spectral difference (green) shows contributions from lipid signals at 1740, 1450, 1370, 1170 and 1065 cm^{-1}, and subtle changes in the carbohydrate region between 1000 and 1170 cm^{-1}. All difference spectra were multiplied by 10.

The hypoxia mimetic drug DMOG reproduces the same spectral signature as hypoxia

The metabolic changes reported above are likely due to the stabilization and activation of HIF in hypoxia and the subsequent transcription of several HIF target genes involved in metabolic reprogramming.[24,45] HIF becomes stabilised in hypoxia due to a reduction in its regulation by the prolyl

hydroxylase enzymes (PHD). Under normoxic conditions, the PHDs hydroxylate HIF on two proline residues, leading to HIF degradation.[10] HIF becomes stabilised under hypoxic conditions because the PHDs require O_2 as a co-factor, therefore one way of chemically mimicking hypoxia is to inhibit PHD activity with pharmacologically active substances such as DMOG. U87MG and D566 glioblastoma cell lines were cultured in the presence of DMOG for 24 h and compared to cells
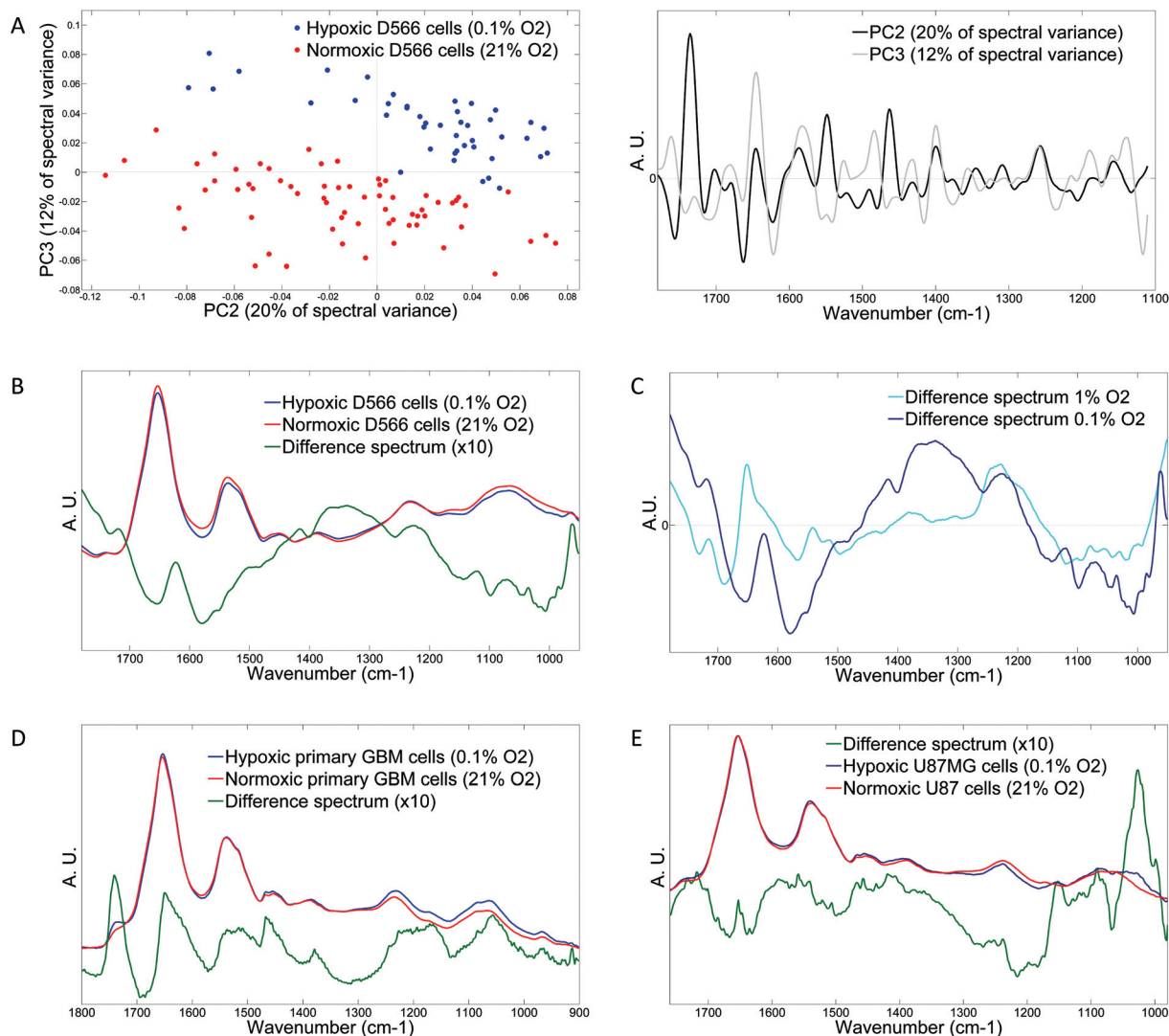
Fig. 2 The infrared signature of cells in severe hypoxia (0.1% O_2) is similar to that of cells at 1% O_2. D566 cells were grown at 0.1 and 21% O_2. The spectra of individual cells were compared by PCA. (A) The PCA score plot shows that hypoxic and normoxic cell spectra can be separated by their spectral signatures along the PC3 axis. PC3 loadings show an increase in peaks at 1740, 1465, and 1380 cm^{-1}, characteristic of lipids in the hypoxic cells. (B) Average and difference spectra of D566 glioblastoma cells after 24 h at 21% (red) and 0.1% (blue) O_2. The spectral difference (green) show changes in the lipids, protein amides I and II, phosphate, and carbohydrate regions. (C) Comparison of difference spectra at 1% and 0.1% O_2 showing their close similarity. The main differences come from variations in baseline deviation and minor changes in the carbohydrate region. (D) Average and difference spectra of primary GBM cells after 24 h at 21% (red) and 0.1% (blue) O_2. The spectral difference (green) shows contributions from lipid signals at 1740, 1450, 1370, 1170 and 1065 cm^{-1}, and changes in the carbohydrate region between 1000 and 1160 cm^{-1}, particularly at 1040 cm^{-1}. This difference spectrum is closely matched to that of 1% O_2 in Fig. 1E. (E) Average and difference spectra of U87MG cells after 24 h at 21% (red) and 0.1% (blue) O_2. The spectral difference (green) shows signals from glycogen (1150, 1080 and 1025 cm^{-1}) and weaker contribution from lipids (1740, 1460 cm^{-1}) and is comparable to that found in Fig. 1B.

grown at 1% and 21% O_2. Spectra of individual cells were recorded at 20×20 μm^2 resolution and compared by PCA and difference spectroscopy. The results for U87MG cells are shown in Fig. 3. In the 900–1800 cm^{-1} region, the PCA score plot (Fig. 3A) shows that normoxic cell spectra are clustered in the negative PC values along the PC1 axis, while most DMOG treated cell spectra are clustered in the positive PC values. Hypoxic cell spectra are located between the normoxic and DMOG treated clusters and among the DMOG cluster. A few DMOG treated and hypoxic cell spectra are clustered further

along the PC1 axis, these cells being extremely rich in glycogen and lipids. The loadings plot shows positive peaks characteristic of lipid (1740, 1465–1450, 1380 cm^{-1}) and carbohydrate (1150, 1080 and 1025 cm^{-1}) accumulation in hypoxia and DMOG treated cells. The carbohydrate profile is evocative of glycogen spectrum as in mild and severe hypoxia. PC1 looks very similar to that of Fig. 1B and accounts for 51% of the spectral variance, evidencing a slightly stronger effect of DMOG over hypoxia on cell chemical composition. In Fig. 3B, the difference spectra between normoxic and DMOG-treated
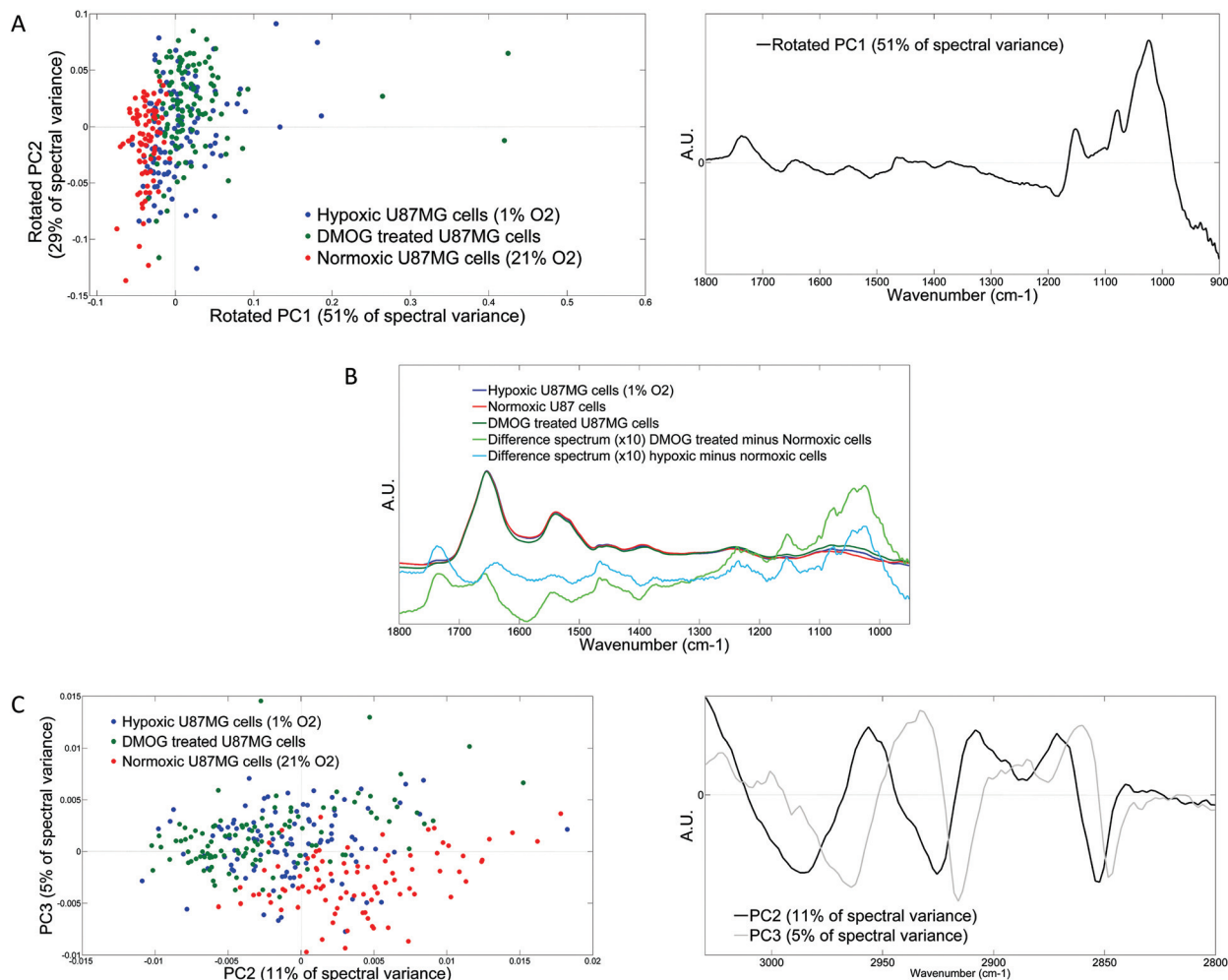
Fig. 3   Effect of the hypoxia mimetic drug DMOG on the chemical composition of U87MG cells. U87MG cells were grown at 21% O_2, 1% O_2 or treated with 0.5 mM DMOG for 24 h. (A) PCA in the 900–1800 cm^{-1} fingerprint region. DMOG-treated and hypoxic cells separate from normoxic cells along the rotated PC1 axis. Some hypoxic and DMOG-treated cells are clustered far along PC1, demonstrating an extreme reaction. Rotated PC1 loading coding for 51% of the spectral variance shows features of lipid and glycogen signals similar to those found in Fig. 1A. The sign of the rotated PC1 loadings is opposite to the sign of the PC1 loadings in Fig. 1A, but interpreted in conjunction with the positive location of the hypoxic and DMOG-treated cells along the rotated PC1 axis in the score plot, this shows that hypoxic and DMOG-treated cells also have increased lipid and glycogen storage in this experience. (B) Average and difference spectra of U87MG cells after 24 h with 21% (red), 1% (blue) O_2, and 0.5 mM DMOG. The spectral difference (green and light blue) shows very similar profiles for glycogen (1150, 1080 and 1025 cm^{-1}), lipids (1740, 1460, and 1380 cm^{-1}) and phosphate features (1235 cm^{-1}). (C) PCA score and loadings plots in the CH region. Normoxic cells separate along the PC3 axis coding for C−H signals from CH_2 acyl chains of fatty acids at 2915 and 2845 cm^{-1}. PC2 also contributes to the separation.

cells, or hypoxic and normoxic cells are shown, further supporting their similar effect on cells. Comparable results were obtained in the CH region (Fig. 3C) where DMOG treated and hypoxic cell spectra were clustered together and separated from normoxic cell spectra along PC2 and PC3 axes coding for an increase in C–H in the hypoxic/DMOG treated cells at 2915, 2925 and 2850 cm^{-1}. Continuity between the hypoxic, normoxic and DMOG treated cell clusters was observed supporting a continuum in the chemical composition of the cells. In D566 cells, the DMOG treated cells were clustered apart from the hypoxic cells on the same PCA axis showing that DMOG effects were of the same nature but stronger than hypoxia at 1% O_2 in this cell line (ESI Fig. S3†). This is in

line with the strong effects of DMOG on HIF nuclear accumulation and target gene transcription.[4] These results demonstrate that the metabolic changes induced by hypoxia and detected by FTIR are likely due the accumulation of HIF and its transcriptional activity. The stronger effects of DMOG compared to hypoxia might be due to the total inhibition of the PHD activity achieved by DMOG treatment compared to the reduced activity obtained by hypoxic incubation at 1 and 0.1% O_2 (50% of activity in 1% O_2 [46]).

Stability of the hypoxic signature over time

We also aimed at assessing the metabolic changes in chronic hypoxia. U87MG, D566 and primary GBM cells were grown in

normoxia and hypoxia (1% O$_2$) up to 120 h and their spectra were recorded and compared by PCA. Results are presented for U87MG cells in Fig. 4, and for D566 and primary GBM cells in ESI Fig. S4 and S5† respectively.

In Fig. 4, the PCA score plots at 24 and 72 h showed that hypoxic and normoxic U87MG cells are separately clustered with a continuum of chemical variations between the 2 clusters as previously shown in Fig. 1A, and ESI Fig. S2A and S3A.† The PCA loadings were similar with an increase in lipid and glycogen signatures in hypoxic cells. The magnitude of the changes did not increase at 72 h with PC1 loadings amounting to 28% of the spectral variance at 72 h and 31% at 24 h. However at 120 h, second derivative spectra had to be used to get rid of the baseline shape variation. The hypoxic and normoxic cell spectra were separated by PC1 coding for 65% of the spectral variance, but separation between the 2 clusters was less marked. No change was observed in the carbohydrate range of the loadings which are dominated by changes in the protein signal.

The separation between normoxic and hypoxic D566 cells was more evident and consistent in the CH range (ESI Fig. S4A–S4C†). Hypoxic and normoxic cell spectra could be separated in PCA score plots at 24, 72 h and 120 h. The spectral signature was an increase in the CH signals from lipids (at 2920 and 2850 cm^{-1}). Small variations in the loading shapes at 120 h were probably related to variations in spectral quality. Separation was less marked after longer hypoxic cultures and the amount of variance between hypoxic and normoxic cells dropped from over 30% at 24 h to 4% at 120 h.

In primary GBM cells, a separation between normoxic and hypoxic cells could be detected for all elapsed time by PCA, using second derivative spectra in the 900–1800 cm^{-1} region (ESI Fig S5A–S5C†). The two clusters were best separated at 24 h. At 120 h the clusters were positioned closer and gave only partial separation (79% of hypoxic spectra and 70% of normoxic spectra were correctly separated). The hypoxic signature evolved with a loss of the contribution from protein at 120 h but an increase of the relative contribution of lipid
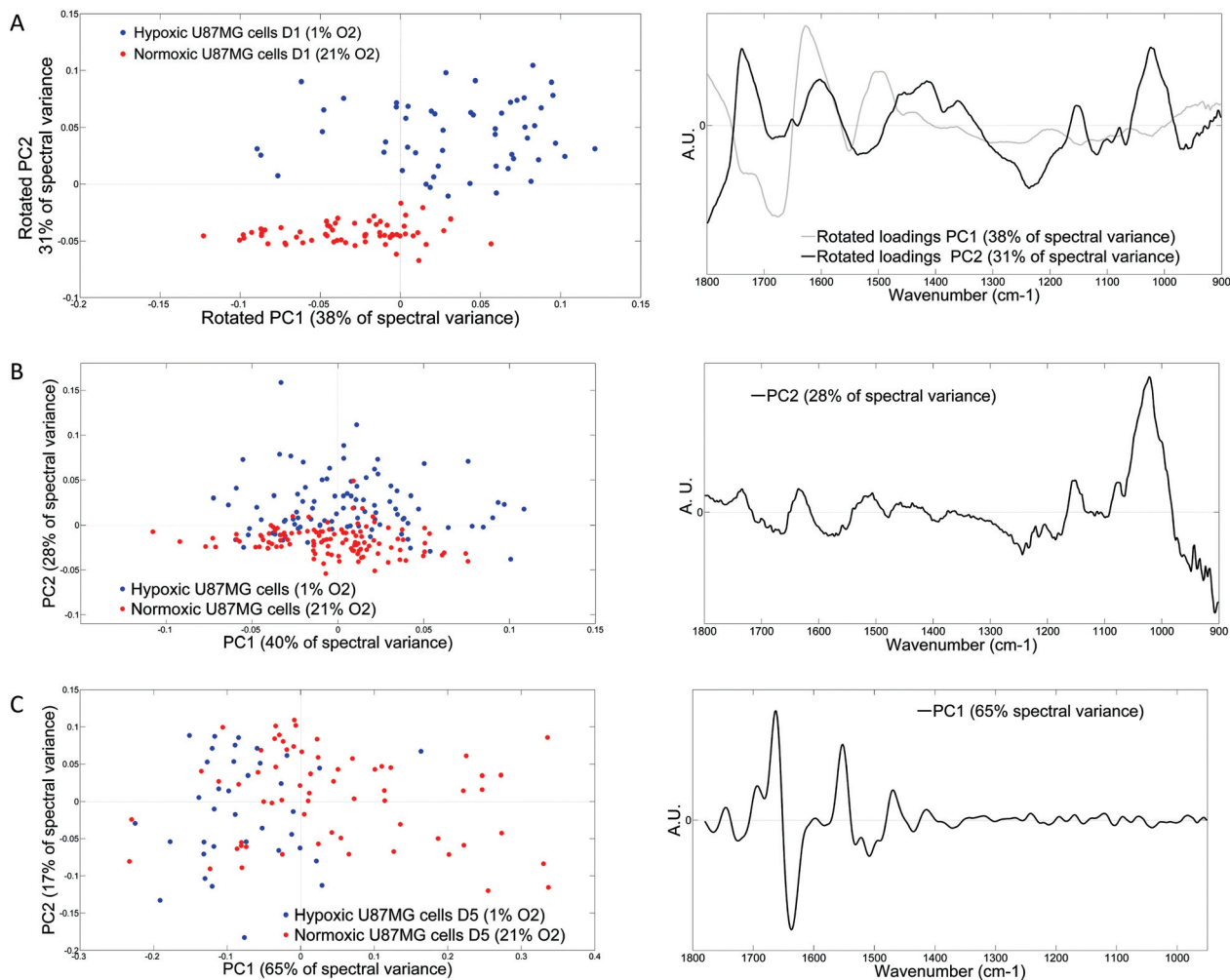

Fig. 4 Evolution of the hypoxic signature over time in U87MG cells. U87MG were cultured in 1% O$_2$ for 24 h, 72 h and 120 h as indicated. (A) PCA score and loadings plot at 24 h. (B) PCA score and loadings plot at 72 h showing the same hypoxic signature at 24 h. (C) PCA score and loadings plot at 120 h showing only a partial separation of hypoxic and normoxic cells and a different spectral signature.

signals (1740, 1471, 1380, 1180 cm^{-1}) in PC1. Contribution from phosphates (1250, 1090 cm^{-1}) and possibly ribose (1120, 1060, 975 cm^{-1}) appeared at 120 h in PC4.

Taken together, the results of the 3 GBM cell lines indicate that the hypoxic signature does not increase with longer incubations in hypoxia, but in fact manifests a slight decrease. This suggests that cells might adapt in chronic hypoxia and maintain a homeostasis that prevents major changes of the chemical composition. In U87MG cells, the disappearance of the glycogen signal may be explained by an enhanced initial glucose uptake, which is transient, and that the primarily stored glucose is used for glycolysis.

Subcellular resolution of the hypoxic signature

It is well known that the infrared spectra of cell nuclei and cytoplasms are different, and it has recently been shown that the perinuclear region containing the endoplasmic reticulum (ER) and Golgi apparatus (GA) also has a specific spectral signature.[41,47] The main differences were found in the CH$_2$: CH$_3$ ratio (from ER/GA and organelle membranes and proteins) and in the phosphate : amide ratio (from nucleic acids and proteins). Since an increase in the lipid signal is one of the main hypoxic signatures detected, we hypothesized that changes in the nuclear : cytoplasmic ratio between individual cells could be a confounding variable in trying to discriminate between normoxic and hypoxic cells. Respiration is essentially a cytoplasmic reaction, whilst the spectrum of a cell is dominated by contributions from the thicker nucleus and perinuclear area. This indicates that it could be more meaningful to record spectra specifically from the cytoplasm. However, oxidative damage triggered by cytoplasmic drugs can also affect the chemical composition of the nucleus as previously shown by Chio-Srichan et al.,[48] hence the recording of spatially resolved information from the nucleus should also be investigated. A synchrotron source allows infrared spectra to be recorded at the diffraction limit (3–25 μm in the mid-infrared), essentially allowing spectra to be recorded at subcellular resolution. As D566 cells are around 50–100 μm in their larger axis and 20 μm on their smaller axis, measuring at 10 × 10 μm^2 spatial resolution allows the recording of spectra from the nucleus or the cytoplasm. We measured D566 cells grown in hypoxia at 1% and 0.1% O$_2$ for 24 h and 120 h. A few spectral maps were also recorded and one of them is shown in Fig. 5. The chemical heterogeneity of a D566 cell is demonstrated by plotting the absorption of specific peaks. The strongest contrasts are observed for lipid peaks (C–H from CH$_2$, C=O from lipids) and phosphates, which illustrates the differences between the nucleus (strong P=O, no C=O) and the perinuclear region (strongest C–H). The carbohydrate signal (COC, COH) is spread throughout the cell. Normalised, averaged spectra from all three cell compartments are shown in Fig. 5G and evidence the differences in the CH and fingerprint regions.

The separation between hypoxic and normoxic cell spectra by PCA was possible with cytoplasmic spectra at 24 h (Fig. 6A) and at 120 h (Fig. 6B), using data in the fingerprint region. It should be noted that separation by PCA was made easier by the use of the spatially resolved data. The spectral signature of hypoxia in the cytoplasm was linked to an increase of lipid contribution in the spectra (1740, 1465, 1380, 1170 cm^{-1}), but changes in the protein signature (amide I and amide II bands), in the phosphates (1250, 1080 cm^{-1}), and in the carbohydrates (1100, 1020 cm^{-1}) were also clearly detected, which was not evidenced in the spectra of the whole cell. The amount of spectral variance (30–40%) between hypoxic and normoxic cell spectra was similar at 24 and 120 h culture and superior to the amount of variance observed for whole cell spectra (12% in Fig. 2). It was also possible to separate the hypoxic and normoxic cell spectra by PCA using the CH range (data not shown).

Surprisingly, a very good separation was also obtained by PCA with nuclear spectra at 24 h (Fig. 6C) and 120 h (Fig. 6D) using the fingerprint region. The spectral signature of hypoxia in the nucleus was remarkably similar to that recorded in the cytoplasm but with a stronger contribution from the protein absorption in the principal component loadings. The protein signal was the dominating contribution in the separation, likely due to the low lipid and high protein concentrations in nuclei. Although the sampled area was smaller than most D566 nuclei, some contribution from the perinuclear region could not be totally avoided due to diffraction and small errors in motorized stage movements, explaining why some lipid contribution was still detected. It was also possible to separate the hypoxic and normoxic cell spectra by PCA using the CH range (data not shown).

In conclusion, using spatially resolved data from the nucleus and cytoplasm allowed a marked improvement in the separation between hypoxic and normoxic cell spectra, especially at 120 h culture. The spectral signature from hypoxia changed in the nuclei compared to the cytoplasms due to a higher contribution of protein signal. This could help achieve a better detection of hypoxic cells, especially for those undergoing weak chemical changes such as D566 cells.

Discussion

Infrared microspectroscopy to detect chemical changes triggered by hypoxia

We have used synchrotron radiation infrared microspectroscopy to investigate the chemical changes that may occur in cells exposed to hypoxia and to reveal that the spectra of cells grown in hypoxia contain subtle chemical composition differences that could be separated by PCA from the spectra of cells grown in normoxia. The spectral signature depends on the cell type, lipid accumulation being a common signature for all cell types. It is detected by changes in the lipid esters (1740 cm^{-1}), phospholipids (1170 cm^{-1}), and methylene (2915, 2850, 1465, 1380 cm^{-1}) infrared bands. These features can potentially be used for detecting hypoxia in tumour cells. Accumulated high levels of glycogen are also observed in hypoxic U87MG. These observations are fully consistent with the metabolic reprogramming induced by hypoxia, with HIF impacting on both
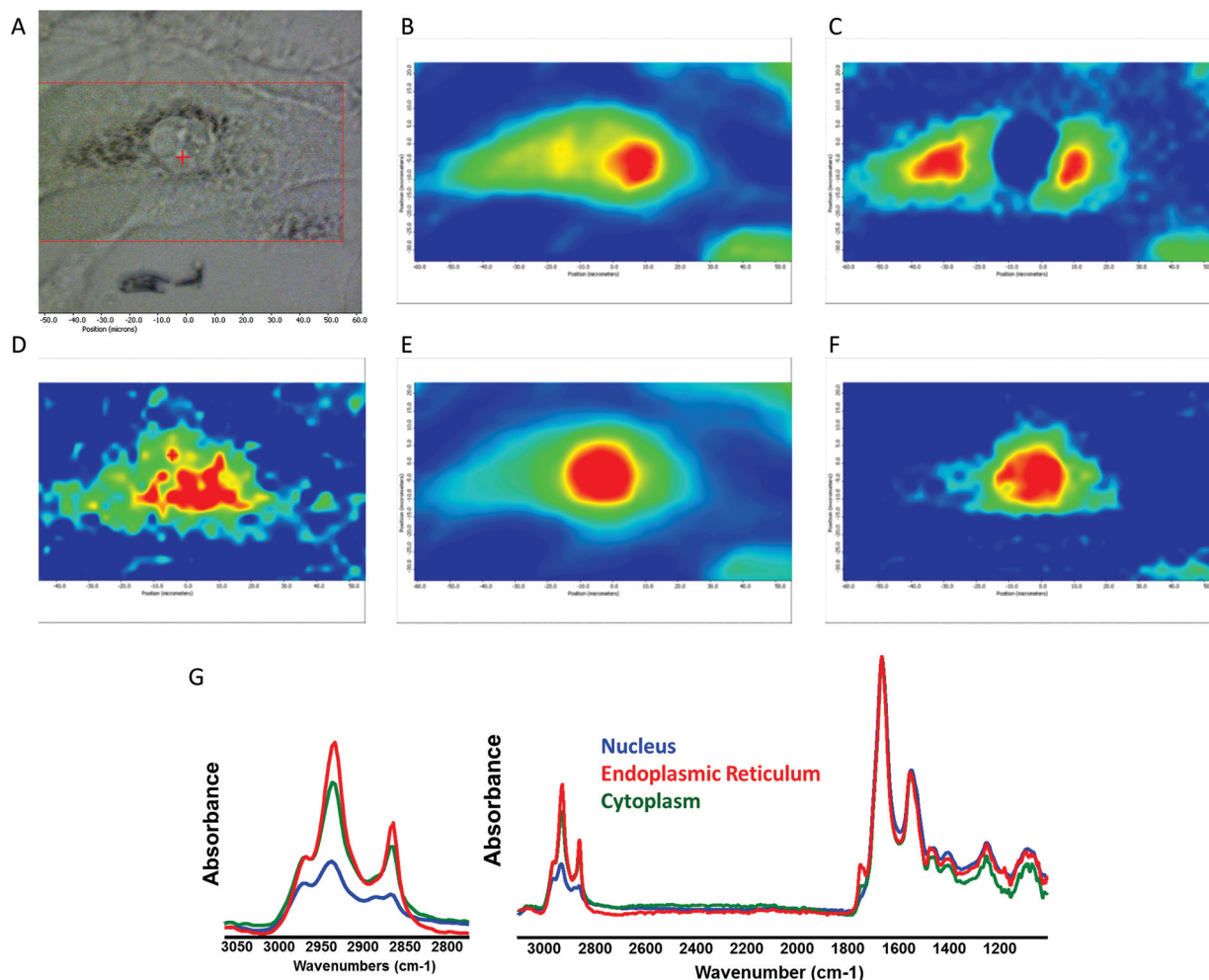
Fig. 5 Heterogeneity in glioblastoma cells mapped at high spatial resolution. (A–F) Example of a D566 cell grown for 24 h at 1% O_2 mapped at 6 × 6 μm^2 resolution. The cell was 116 μm in length. (A) Bright field micrograph. The distribution of (B) CH_2 from aliphatic lipids, (C) $C{=}O$ from lipid esters, (D) C−O and P$=$O from polysaccharides and nucleic acids, (E) amide I from protein, and (F) P$=$O from nucleic acids and proteins, illustrate the heterogeneity between the nucleus, the cytoplasm and the perinuclear region. (G) Average spectra from the nuclear (blue), perinuclear (red) and cytoplasmic (green) regions show large differences in the CH (2800–3000 cm^{-1}) and fingerprint regions C$=$O (1740 cm^{-1}), P$=$O (1240 cm^{-1}) and C−O (1000–1180 cm^{-1}) contributions within one cell. Spectra were normalized to the amide I intensity.

cellular anabolism (glycogen and lipid synthesis) and catabolism (glycolysis)[49,50] (for a review see ref. 1). This was further confirmed by the induction of HIF by DMOG (Fig. S6†) which gave the same spectral signatures than cultures in hypoxia in the two cell lines investigated. These results constitute the first demonstration that cell infrared spectra can be used to discriminate between hypoxic and normoxic cells. Only one similar study has been published previously, by Petibois *et al.*, who studied cell extracts and supernatant media from U87MG and A549/8 cells cultured in hypoxia and normoxia.[51] The authors found differences in lactic acid and glucose concentrations, in addition to changes in lipid peroxidation triggered by hypoxia. Surprisingly, a decrease in the $CH_2 : CH_3$ ratio under hypoxic conditions (3% O_2) was reported, while under our culture conditions (1% and 0.1% O_2) an increase in the CH_2 peaks under hypoxic conditions was always detected, in agreement with the fact that hypoxic cells accumulate lipid

droplets in their cytoplasm. Also, in contrast to our results, no change in glycogen levels was reported in U87MG cells. These inconsistencies are likely to come from the fact that we measured the whole cell composition directly while Petibois *et al.*, worked on cell extracts and conditioned culture medium after cell removal. Moreover, the extensive use of curve fitting procedures in their study and the lack of multivariate statistical analysis are not the best appropriate approach for data analysis.

Hypoxic hallmarks and inter/intra-tumoural variations

The increase in cell lipids under hypoxic conditions was modest, yet clear and consistent for all 4 cell types studied. This could therefore constitute a robust hypoxic hallmark. Magnetic resonance spectroscopy has previously been used in the C6 rat glioma model to investigate changes in lipids, which were reported in cells experiencing severe prenecrotic hypoxia.[52–54] Nevertheless, FTIR measurements for hypoxia
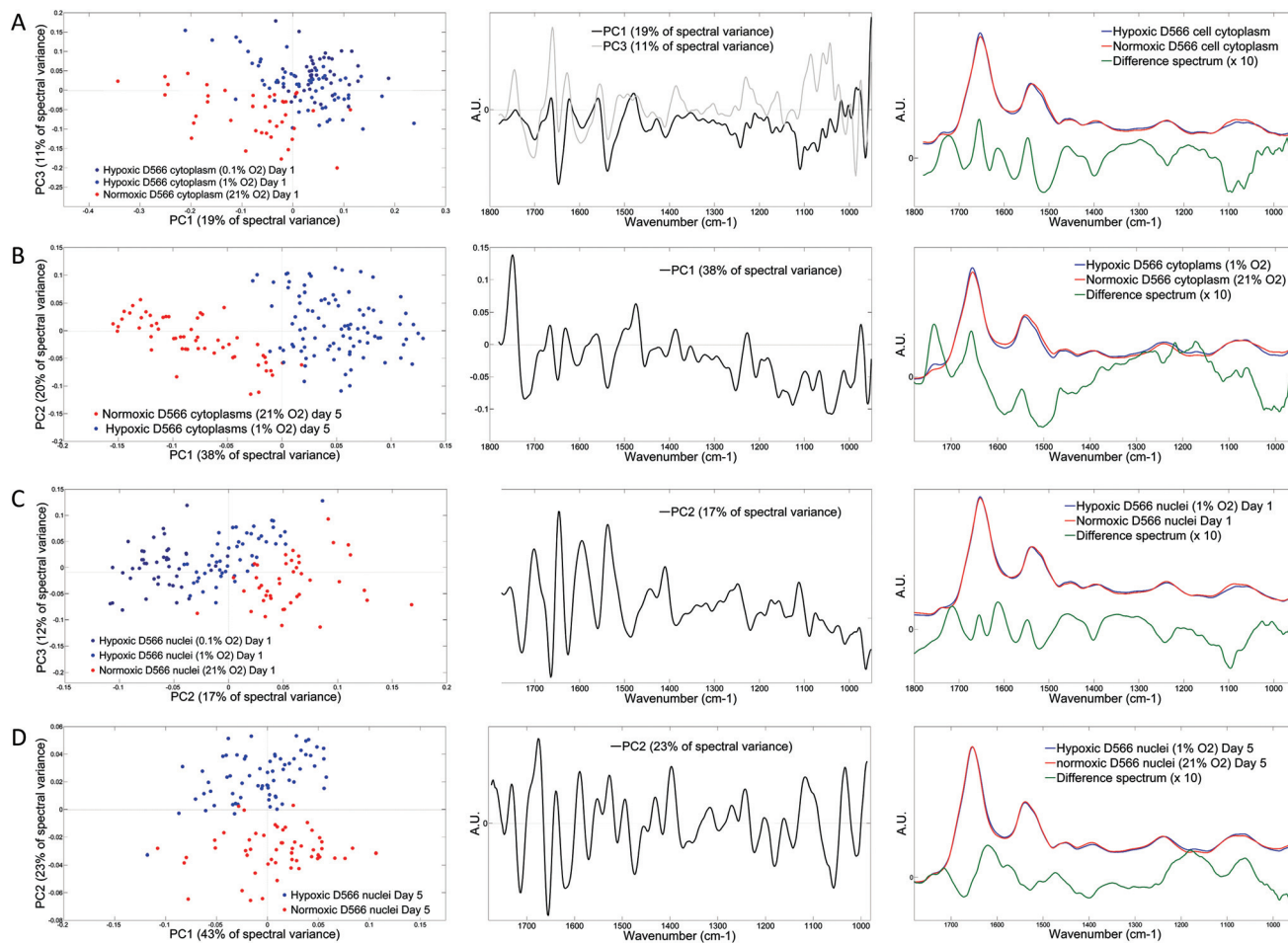
Fig. 6 Spatially resolved data improve the separation between hypoxic and normoxic cell spectra at every time-point. (A) Spectra of normoxic and hypoxic D566 cell cytoplasms at day 1 can be separated by PCA. PCA score plot, loadings of PC1 and PC2 capturing a cumulative 30% of the spectral variance, average and difference spectra. (B) Spectra of normoxic and hypoxic D566 cell nuclei at day 1 can be separated by PCA. PCA score plot, loadings of PC2 coding for 17% of spectral variance, average and difference spectra. (C) Spectra of normoxic and hypoxic D566 cytoplasms at day 5 separated by PCA. PCA score plot, loadings of PC1 coding for 38% of the spectral variance, average and difference spectra. (D) Spectra of normoxic and hypoxic D566 cell nuclei at day 5 separated by PCA. PCA score plot, PC2 loadings coding for 23% of spectral variance, average and difference spectra.

detection in brain tumours might be challenging in a clinical set-up, due to the large variations in lipid signals in brain tissue. This is due to the presence of different cell types with various levels of sphingolipids, phospholipids, and myelin.[55–58] Gaigneaux *et al.* reported the infrared spectra of 9 glioma cell lines (including U87MG) and whilst no large variation in lipid levels were detected between the cell lines, they did however find correlations between wavenumbers in the CH region and their *in vitro* migration and *in vivo* aggressiveness.[59] We also observed variations in the carbohydrate signal which were particularly strong in U87MG cells where accumulation of glycogen was detected at levels comparable to those found in hepatocytes[40] and stem cells.[28] This could be due to differences in glucose uptake and metabolism and varying rates of glycolysis between cell types. Hypoxia induces the expression of genes encoding the enzymes required to convert glucose to glycogen, including hexokinase (HK1 or HK2), phosphogluco-

mutase 1 (PGM1), UDP-glucose pyrophosphorylase (UGP2), glycogen synthase (GYS1), glycogen branching enzyme (GBE1), as well as the gene encoding PPP1R3C, which activates GYS1 and inhibits liver-type glycogen phosphorylase (PYGL), the enzyme that breaks down glycogen.[11] PYGL is expressed in U87MG cells, and its knockdown increases glycogen accumulation.[60] Similarly, phosphoglucomutase 1 is overexpressed several fold in hypoxic U7MG cells.[61]

Robustness of the FTIR chemical signatures

As expected, the infrared signature of hypoxia was related to the main macromolecules and no changes from small metabolites such as ATP, ADP, pyruvate or lactate could be detected. There was no clear difference between the hypoxic signature of cells exposed to mild or severe hypoxia and the hypoxic signature did not evolve strongly over time. This suggests that hypoxic cells adopt a metabolic fingerprint that is stable and

precisely regulated. The fact that different levels and durations of hypoxia have very similar spectral signatures may make it easier to interpret the hypoxic signature in tissues. We observed that the hypoxic signature becomes weaker after longer periods which may imply that it will be more difficult to detect in tumours that have been in hypoxia for an extended time period. Nevertheless, hypoxic episodes in tumours have been shown to be highly dynamic with cycles of hypoxia and reoxygenation,[62–64] indicating that tumour cells might never experience long periods of hypoxic exposure without episodes of re-oxygenation. Our results highlight the potential of FTIR for tumour hypoxia detection in patient samples. We never observed complete separation between the hypoxic and normoxic spectra clusters, indicating that there is a continuum of chemical states between hypoxic and the normoxic cells. This could be due to the fact that some cells in normoxic cultures exist in an endogenous hypoxic state induced by mitochondrial respiration as shown by Prior et al.[65] Conversely, some cells grown in hypoxia may have managed to preserve a normoxic phenotype by more efficient scavenging of oxygen.

We have shown that spatially resolved data recorded either in the nucleus or the cytoplasm of cells allowed separation of hypoxic and normoxic D566 cells even after long culture durations. The signature found in the nucleus showed a stronger contribution of protein-related signals than the cytoplasm. This could potentially be linked to changes in histone methylation/acetylation patterns[60,66] as histones are the major type of protein found in the nucleus.

Conclusion

The combination of synchrotron radiation FTIR microspectroscopy and multivariate statistical analysis has allowed identification of an increase in lipids in glioblastoma cells as an intrinsic marker of hypoxia. This signature was detected in cells grown under low oxygen conditions without the need for external markers, thus avoiding any problems associated with dye penetration, or antibody quality and reproducibility. Hence such an approach used here in cell lines, may in the future be applicable to glioblastoma tissue samples in which it is necessary to detect hypoxia for grading, staging and prognosis purposes. Synchrotron radiation FTIR microspectroscopy with its high brilliance is intrinsically well adapted for analysing single cells and even subcellular compartments, a mandatory requirement to study organelle specific events such as mitochondrial respiration and cytoplasmic metabolism. It is also well adapted to study the heterogeneous nature of tumours with regions of normoxia, transient and chronic hypoxia.

Notes and references

1 M. C. Brahimi-Horn, G. Bellot and J. Pouysségur, *Curr. Opin. Genet. Dev.*, 2011, **21**, 67–72.

2 K. Steinestel, S. Eder, A. Schrader and J. Steinestel, *Clin. Transl. Med.*, 2014, **3**, 17.

3 G. Zhou, L. A. Dada, M. Wu, A. Kelly, H. Trejo, Q. Zhou, J. Varga and J. I. Sznajder, *Am. J. Physiol.: Lung Cell. Mol. Physiol.*, 2009, **297**, L1120–L1130.

4 A. Herrmann, M. Rice, R. Lévy, B. L. Pizer, P. D. Losty, D. Moss and V. Sée, *Oncogenesis*, 2015, **4**, e138.

5 R. Bos, P. van der Groep, A. E. Greijer, A. Shvarts, S. Meijer, H. M. Pinedo, G. L. Semenza, P. J. van Diest and E. van der Wall, *Cancer*, 2003, **97**, 1573–1581.

6 a. W. Eckert, M. Kappler, J. Schubert and H. Taubert, *J. Oral Maxillofac. Surg.*, 2012, **16**, 189–196.

7 K.-Z. Liu, A. Man, R. A. Shaw, B. Liang, Z. Xu and Y. Gong, *Biochim. Biophys. Acta*, 2006, **1758**, 960–967.

8 D. J. Brat and E. G. Van Meir, *Lab. Invest.*, 2004, **84**, 397–405.

9 P. Province, C. E. Griguer, X. Han, L. B. Nabors and H. F. Shaykh, in *Evolution of the Molecular Biology of Brain Tumors and the Therapeutic Implications*, ed. T. Lichtor, 2013.

10 G. L. Semenza, *Cell*, 2012, **148**, 399–408.

11 G. L. Semenza, *J. Clin. Invest.*, 2013, **123**, 3664–3671.

12 A. C. Begg, *Int. J. Radiat. Oncol., Biol., Phys.*, 2003, **56**, 917–919.

13 J. Bagnall, J. Leedale, S. E. Taylor, D. G. Spiller, M. R. H. White, K. J. Sharkey, R. N. Bearon and V. See, *J. Biol. Chem.*, 2014, **289**, 5549–5564.

14 F. Agani and B.-H. Jiang, *Curr. Cancer Drug Targets*, 2013, **13**, 245–251.

15 H. A. Haeberle, C. Dürrstein, P. Rosenberger, Y. M. Hosakote, J. Kuhlicke, V. A. J. Kempf, R. P. Garofalo and H. K. Eltzschig, *PLoS One*, 2008, **3**, e3352.

16 J. Patel, K. Landers, R. H. Mortimer and K. Richard, *Placenta*, 2010, **31**, 951–957.

17 A. Mayer, M. Höckel and P. Vaupel, *Adv. Exp. Med. Biol.*, 2008, **614**, 127–136.

18 R. A. Jonathan, K. I. Wijffels, W. Peeters, P. C. de Wilde, H. A. Marres, M. A. Merkx, E. Oosterwijk, A. J. van der Kogel and J. H. Kaanders, *Radiother. Oncol.*, 2006, **79**, 288–297.

19 J. Bussink, J. H. a. M. Kaanders and A. J. van der Kogel, *Radiother. Oncol.*, 2003, **67**, 3–15.

20 L. Goethals, A. Debucquoy, C. Perneel, K. Geboes, N. Ectors, H. De Schutter, F. Penninckx, W. H. McBride, A. C. Begg and K. M. Haustermans, *Int. J. Radiat. Oncol., Biol., Phys.*, 2006, **65**, 246–254.

21 A. M. Weljie and F. R. Jirik, *Int. J. Biochem. Cell Biol.*, 2011, **43**, 981–989.

22 R. A. Gatenby and R. J. Gillies, *Nat. Rev. Cancer*, 2004, **4**, 891–899.

23 G. Laurenti, E. Benedetti, B. D'Angelo, L. Cristiano, B. Cinque, S. Raysi, M. Alecci, M. P. Cerù, M. G. Cifone, R. Galzio, A. Giordano and A. Cimini, *J. Cell. Biochem.*, 2011, **112**, 3891–3901.

24 S. E. Rademakers, P. N. Span, J. H. a. M. Kaanders, F. C. G. J. Sweep, A. J. van der Kogel and J. Bussink, *Mol. Oncol.*, 2008, **2**, 41–53.

25 F. Le Naour, M.-P. Bralet, D. Debois, C. Sandt, C. Guettier, P. Dumas, A. Brunelle and O. Laprévote, *PLoS One*, 2009, **4**, e7408.

26 F. Le Naour, C. Sandt, C. Peng, N. Trcera, F. Chiappini, A.-M. Flank, C. Guettier and P. Dumas, *Anal. Chem.*, 2012, **84**, 10260–10266.

27 V. W. Petit, M. Réfrégiers, C. Guettier, F. Jamme, K. Sebanayakam, A. Brunelle, O. Laprévote, P. Dumas and F. Le Naour, *Anal. Chem.*, 2010, **82**, 3963–3968.

28 C. Sandt, O. Féraud, N. Oudrhiri, M. L. Bonnet, M. C. Meunier, Y. Valogne, A. Bertrand, M. Raphaël, F. Griscelli, A. G. Turhan, P. Dumas and A. Bennaceur-Griscelli, *PLoS One*, 2012, **7**, e30743.

29 B. Bird, M. J. Romeo, M. Diem, K. Bedrossian, N. Laver and S. Naber, *Vib. Spectrosc.*, 2008, **48**, 101–106.

30 O. Uckermann, R. Galli, M. Anger, C. Herold-Mende, E. Koch, G. Schackert, G. Steiner and M. Kirsch, *Int. J. Radiat. Biol.*, 2014, **90**, 710–717.

31 N. Jamin, L. Miller, J. Moncuit, W. H. Fridman, P. Dumas and J. L. Teillaud, *Biopolym. – Biospectroscopy Sect.*, 2003, **72**, 366–373.

32 K. Z. Liu and H. H. Mantsch, *J. Mol. Struct.*, 2001, **565–566**, 299–304.

33 S. Boydston-White, M. Romeo, T. Chernenko, A. Regina, M. Miljković and M. Diem, *Biochim. Biophys. Acta*, 2006, **1758**, 908–914.

34 F. Bonnier, S. Rubin, L. Ventéo, C. M. Krishna, M. Pluot, B. Baehrel, M. Manfait and G. D. Sockalingum, *Biochim. Biophys. Acta*, 2006, **1758**, 968–973.

35 J. Dulinska, Z. Setkowicz, K. Janeczko, C. Sandt, P. Dumas, L. Uram, K. Gzielo-Jurek and J. Chwiej, *Anal. Bioanal. Chem.*, 2012, **402**, 2267–2274.

36 W. André, C. Sandt, P. Dumas, P. Djian and G. Hoffner, *Anal. Chem.*, 2013, **85**, 3765–3773.

37 P. Dumas, F. Polack, B. Lagarde, O. Chubar, J. L. Giorgetta and S. Lefrançois, *Infrared Phys. Technol.*, 2006, **49**, 152–160.

38 M. Höckel and P. Vaupel, *J. Natl. Cancer Inst.*, 2001, **93**, 266–276.

39 A. Carreau, B. El Hafny-Rahbi, A. Matejuk, C. Grillon and C. Kieda, *J. Cell. Mol. Med.*, 2011, **15**, 1239–1253.

40 F. Le Naour, C. Sandt, C. Peng, N. Trcera, F. Chiappini, A.-M. Flank, C. Guettier and P. Dumas, *Anal. Chem.*, 2012, **84**, 10260–10266.

41 C. Sandt, J. Frederick and P. Dumas, *J. Biophotonics*, 2013, **6**, 60–72.

42 K. M. A. Pereira, F. N. Chaves, T. S. A. Viana, F. S. R. Carvalho, F. W. G. Costa, A. P. N. N. Alves and F. B. Sousa, *Oncol. Lett.*, 2013, **6**, 311–316.

43 E. Favaro, K. Bensaad, M. G. Chong, D. a. Tennant, D. J. P. Ferguson, C. Snell, G. Steers, H. Turley, J.-L. Li, U. L. Günther, F. M. Buffa, A. McIntyre and A. L. Harris, *Cell Metab.*, 2012, **16**, 751–764.

44 S. M. Evans, K. D. Judy, I. Dunphy, W. Timothy Jenkins, W. T. Hwang, P. T. Nelson, R. A. Lustig, K. Jenkins, D. P. Magarelli, S. M. Hahn, R. A. Collins, S. Grady and C. J. Koch, *Clin. Cancer Res.*, 2004, **10**, 8177–8184.

45 G. L. Semenza, *Physiol.*, 2009, **24**, 97–106.

46 D. P. Stiehl, R. Wirthner, J. Köditz, P. Spielmann, G. Camenisch and R. H. Wenger, *J. Biol. Chem.*, 2006, **281**, 23482–23491.

47 S. Clède, C. Policar and C. Sandt, *Appl. Spectrosc.*, 2014, **68**, 113–117.

48 S. Chio-Srichan, M. Réfrégiers, F. Jamme, S. Kascakova, V. Rouam and P. Dumas, *Biochim. Biophys. Acta*, 2008, **1780**, 854–860.

49 N. Pescador, D. Villar, D. Cifuentes, M. Garcia-Rocha, A. Ortiz-Barahona, S. Vazquez, A. Ordoñez, Y. Cuevas, D. Saez-Morales, M. L. Garcia-Bermejo, M. O. Landazuri, J. Guinovart and L. del Peso, *PLoS One*, 2010, **5**, e9644.

50 J. Krishnan, M. Suter, R. Windak, T. Krebs, A. Felley, C. Montessuit, M. Tokarska-Schlattner, E. Aasum, A. Bogdanova, E. Perriard, J.-C. Perriard, T. Larsen, T. Pedrazzini and W. Krek, *Cell Metab.*, 2009, **9**, 512–524.

51 C. Petibois, B. Drogat, A. Bikfalvi, G. Déléris and M. Moenner, *FEBS Lett.*, 2007, **581**, 5469–5474.

52 S. Zoula, P. F. J. W. Rijken, J. P. W. Peters, R. Farion, B. P. J. Van der Sanden, A. J. Van der Kogel, M. Décorps and C. Rémy, *Br. J. Cancer*, 2003, **88**, 1439–1444.

53 C. Rémy, N. Fouilhé, I. Barba, N. Fouilhã, E. Sam-lal, H. Lahrech, M. Izquierdo, A. Moreno, A. Ziegler, R. Massarelli and M. Dã, *Cancer Res.*, 1997, 407–414.

54 X. Li, D. B. Vigneron, S. Cha, E. E. Graves, F. Crawford, S. M. Chang and S. J. Nelson, *Am. J. Neuroradiol.*, 2005, **26**, 760–769.

55 I. Dreissig, S. Machill, R. Salzer and C. Krafft, *Spectrochim. Acta., Part A*, 2009, **71**, 2069–2075.

56 J. Chwiej, J. Dulinska, K. Janeczko, P. Dumas, D. Eichert, J. Dudala and Z. Setkowicz, *J. Chem. Neuroanat.*, 2010, **40**, 140–147.

57 N. Amharref, A. Beljebbar, S. Dukic, L. Venteo, L. Schneider, M. Pluot, R. Vistelle and M. Manfait, *Biochim. Biophys. Acta*, 2006, **1758**, 892–899.

58 S. Caine, P. Heraud, M. J. Tobin, D. McNaughton and C. C. A. Bernard, *Neuroimage*, 2012, **59**, 3624–3640.

59 A. Gaigneaux, C. Decaestecker, I. Camby, T. Mijatovic, R. Kiss, J. M. Ruysschaert and E. Goormaghtigh, *Exp. Cell Res.*, 2004, **297**, 294–301.

60 X. Wu, J. Sun and L. Li, *Neurosci. Bull.*, 2013, **29**, 685–692.

61 R. Blum, J. Jacob-Hirsch, N. Amariglio, G. Rechavi and Y. Kloog, *Cancer Res.*, 2005, **65**, 999–1006.

62 P. J. Speicher, G. M. Beasley, B. Jiang, M. E. Lidsky, G. M. Palmer, P. M. Scarbrough, P. J. Mosca, M. W. Dewhirst and D. S. Tyler, *Ann. Surg. Oncol.*, 2014, **21**, 1435–1440.

63 A. Lal, H. Peters, B. St Croix, Z. A. Haroon, M. W. Dewhirst, R. L. Strausberg, J. H. A. M. Kaanders, A. J. Van Der Kogel and G. J. Riggins, *J. Natl. Cancer Inst.*, 2001, **93**, 1337–1343.

64 C.-T. Lee, M.-K. Boss and M. W. Dewhirst, *Antioxid. Redox Signaling*, 2014, **21**, 313–337.

65 S. Prior, A. Kim, T. Yoshihara, S. Tobita, T. Takeuchi and M. Higuchi, *PLoS One*, 2014, **9**.

66 H. Chen, Y. Yan, T. L. Davidson, Y. Shinkai and M. Costa, *Cancer Res.*, 2006, **66**, 9009–9016.